stable clusters. However, in contrast to C_{60}, the metallic Ti atoms in Ti_8C_{12} not only stabilize the structure composed entirely of pentagons but also give it a unique electronic structure that is characterized by the Fermi energy lying in the middle of the band. One therefore does not have to dope a met-car to make it conducting as is necessary for C_{60} (*13*).

REFERENCES AND NOTES

1. B. C. Guo, K. P. Kerns, A. W. Castleman, Jr., *Science* **255**, 1411 (1992); *J. Phys. Chem.*, in press.
2. R. F. Curl and R. E. Smalley, *Sci. Am.* **265**, 54 (October 1991); H. W. Kroto, J. R. Heath, S. C. O'Brien, R. E. Curl, R. E. Smalley, *Nature* **318**, 162 (1985).
3. P. Hohenberg and W. Kohn, *Phys. Rev.* **136**, B864 (1964); W. Kohn and L. J. Sham, *ibid.* **140**, A1133 (1965).
4. D. E. Ellis, *Int. J. Quantum Chem.* **S2**, 35 (1968); M. R. Press, S. N. Khanna, P. Jena, *Phys. Rev. B* **36**, 5446 (1987).
5. J. L. Martins, J. Buttet, R. Car, *Phys. Rev. B* **31**, 1804 (1985); F. Reuse, S. N. Khanna, V. de Coulon, J. Buttet, *ibid.* **41**, 11743 (1990).
6. G. B. Bachelet, D. R. Hamann, M. Schluter, *ibid.* **26**, 4199 (1982).
7. W. B. Pearson, Ed., *A Handbook of Lattice Spacings and Structures of Metals and Alloys* (Pergamon, New York, 1967).
8. F. Liu, S. N. Khanna, P. Jena, *Phys. Rev. B* **43**, 8179 (1991).
9. M. R. Press, S. N. Khanna, P. Jena, M. J. Puska, *Z. Phys. B* **81**, 281 (1990).
10. C. S. Yannoni, P. Bernier, D. S. Bethune, G. Meijer, J. R. Salem, *J. Am. Chem. Soc.* **113**, 3190 (1991).
11. S. Saito and A. Oshiyama, *Phys. Rev. Lett.* **66**, 2637 (1991).
12. J. H. Weaver *et al.*, *ibid.*, p. 1741.
13. M. J. Rosseinsky *et al.*, *ibid.*, p. 2830.

14. This work was funded in part by a grant from the Department of Energy (DE-FG05-87ER45316). One of the authors (B.V.R.) is supported by the Army Research Office (DAAL-03-89-K-0015) for work in magnetism. We thank A. W. Castleman, Jr., for sharing his results. One of us (S.N.K.) is grateful to F. Reuse and J. L. Martins for help in local density calculations. We are grateful to B. B. Brown and other members of Academic Computing for the computational facilities.

20 July 1992; accepted 21 September 1992

Temperature and Size Variabilities of the Western Pacific Warm Pool

Xiao-Hai Yan,* Chung-Ru Ho, Quanan Zheng, Vic Klemas

Variabilities in sea-surface temperature and size of the Western Pacific Warm Pool were tracked with 10 years of satellite multichannel sea-surface temperature observations from 1982 to 1991. The results show that both annual mean sea-surface temperature and the size of the warm pool increased from 1983 to 1987 and fluctuated after 1987. Possible causes of these variations include solar irradiance variabilities, El Niño–Southern Oscillation events, volcanic activities, and global warming.

The Western Pacific Warm Pool (WPWP) covers more of the earth's surface than does the continental United States. It stands out vividly as the orange and red area in our newly processed image of long-term average sea-surface temperature (SST) obtained from satellite data (Fig. 1). This swath of ocean near New Guinea has a temperature consistently higher than 28°C (*1*), about 2° to 5°C higher than that of other equatorial waters, and is the largest single expanse of warm water on our planet.

In recent years, significant international efforts have been made to understand the coupled atmosphere system in the equatorial ocean. However, most oceanographic studies have focused on the eastern and central Pacific Ocean with less effort given to the WPWP, although the early stages of the El Niño–Southern Oscillation (ENSO) phenomenon may first develop there (*2*). Therefore, it is important to track the warm pool as its temperature and size fluctuate from year to year and to understand the relation of these dynamics and ENSO events to global climate changes. To track the changes in the WPWP, we analyzed multichannel SST (MCSST) data from the Television and Infrared Observation Satellite–National Oceanic and Atmospheric Administration (TIROS-N–NOAA) series Advanced Very High Resolution Radiometer (AVHRR). This MCSST product consists of a weekly composite of the globe and regional subsets at a resolution of $\sim$18 km. We used the weekly MCSST for the tropical Pacific Ocean from 1982 to 1991 to compute monthly mean SST, annual mean SST, and long-term mean SST.

The TIROS-N–NOAA series polar orbiting satellites carry four-channel (TIROS-N, NOAA-6, NOAA-8, and NOAA-10) or five-channel (NOAA-7 and NOAA-9) AVHRR sensors. Each sensor has an instantaneous field of view that corresponds to a ground resolution of about 1.1 km at nadir as well as a total scan field of view of ±55.4° from nadir (approximately 2240 km). The five spectral bands measured are as follows: channel 1, visible, 0.58 to 0.68 μm; channel 2, near infrared, 0.725 to 1.10 μm; channel 3, infrared, 3.55 to 3.99 μm; channel 4, thermal infrared, 10.2 to 11.5 μm; and channel 5, thermal infrared, 11.5 to 12.5 μm (NOAA-7 and NOAA-9).

MCSST values are binned into 2048 by 1025 pixel grids. Then, for each grid point the average of all MCSST measurements available for 1 week is computed. Open areas are interpolated with an iterative Laplacian relaxation technique until all such areas connected to valid observations are filled. A first estimate for open areas is provided by computation of the mean of horizontal, bounding data-filled pixels. The original global weekly MCSST data are 16 bits, and the temperatures are these values divided by 10. Thus, the resolution of MCSST is 0.1°C with an overall calibration error of ±0.2°C (*3*). The weekly MCSST is first averaged into monthly mean MCSST. The annual mean MCSST and long-term mean MCSST are then averaged again from monthly mean and annual mean MCSST, respectively.

Figure 1 shows the vast WPWP, which has the highest open-ocean water temperatures in the world. The pattern of the long-term mean SST from calibrated satellite AVHRR data is close to that of the obser-

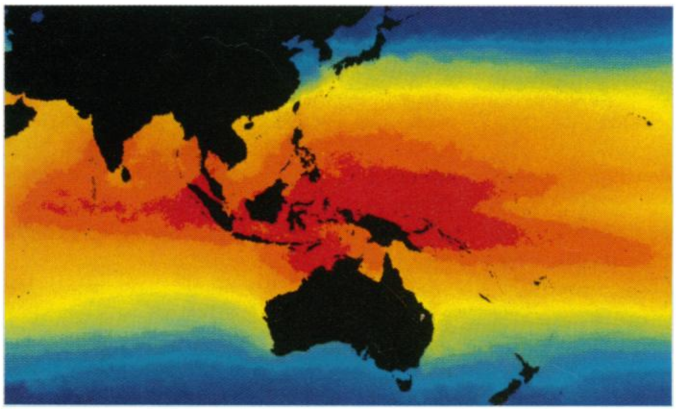

Fig. 1. Color-enhanced image of 10-year mean (1982 to 1991) SST from satellite data, with warmest surface temperature evident in the WPWP (orange and red).

Center for Remote Sensing, Graduate College of Marine Studies, University of Delaware, Newark, DE 19716.

*To whom correspondence should be addressed.

Fig. 2. Color-enhanced image of WPWP SST from 1982 to 1991.

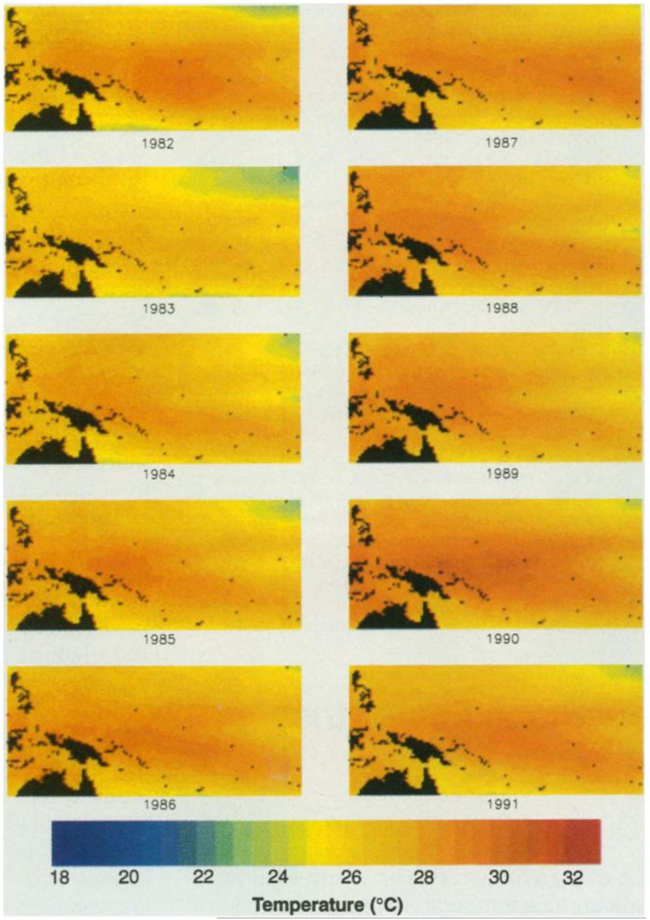

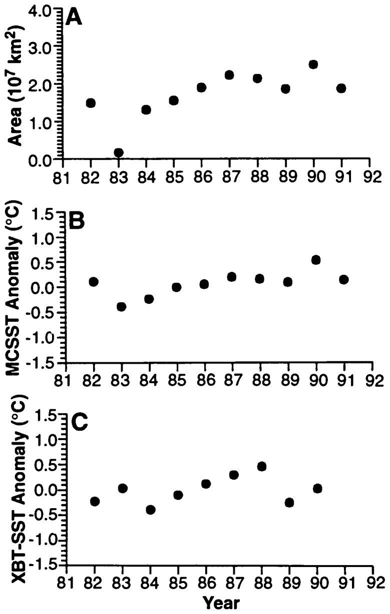

Fig. 3. (**A**) Time series of WPWP area between 1982 and 1991 calculated from satellite data. (**B**) Time series of WPWP SST between 1982 and 1991 calculated from satellite data. (**C**) Time series of WPWP SST between 1982 and 1990 from VOS XBTs.

vation data gathered at sea level, especially in the WPWP (4).

We tracked the WPWP using data from 1982 to 1991 as its temperature and size fluctuated (Fig. 2). A slow warming trend of the WPWP water and a gradual increase of the pool size are evident. To analyze the trends observed from 10 years of satellite data, we computed and plotted the time series of the size of the WPWP, which was defined as an area in which SST was higher than 28°C inside a rectangular box from 120°E to 150°W and from 20°S to 20°N (Fig. 3A). In a similar fashion, we computed and plotted the annual mean area anomaly of the averaged warm pool temperature using all pixels in this area (Fig. 3B). Satellite data revealed that the SST in the WPWP and the size of this area increased monotonically from 1983 to 1987. However, the SST and size of the pool fluctuated after 1987. Possible causes of the size and temperature shifts include (i) solar irradiance variability during the recent transition between solar activity cycles 21 and 22, (ii) ENSO events in 1982 to 1983, 1986 to 1987, and 1991 to 1992, (iii) biases in the data caused by aerosols from the volcanic eruptions of El Chichon and Mount Pinatubo, and (iv) global warming.

A previous study showed the relation between solar irradiance and SST. Reid (5, 6) put forth a sun-climate theory that relates the envelope of the 11-year cycle of solar activity to variations in SST. However, Kelly and Wrigley (7) questioned the significance of his correlative study results. Apparently, data from these studies cannot resolve the question of solar forcing.

In the past 10 years, there have been three ENSO events: 1982 to 1983 (the largest of the century), 1986 to 1987, and 1991 to 1992. As the 1982 ENSO event progressed, warm water from the western tropical Pacific moved eastward. In addition, temperature in the WPWP may have been cooler, and the dips in the curves in Fig. 3, A and B, for 1983 and 1991 may reflect these ENSO events. However, there was no such signal in the temperature curve in 1986 and 1987, which suggests that signals in satellite SSTs may be due not only to ENSO anomalies but also to the other factors.

In 1982 and 1991, the El Chichon and Mount Pinatubo volcanoes erupted, sending massive amounts of sulfur-based aerosols into the stratosphere. These aerosols initially spread around the globe as two bands centered on the latitude of their respective volcanoes. However, they then spread out latitudinally, with substantial amounts covering the equatorial belt (8). This aerosol material blocked the sunlight and caused a true temperature decrease and an error in the MCSST operational retrievals. The cooling in 1983 and 1991 (Fig. 3, A and B) is quite likely associated with these eruptions. However, aside from those periods, a slow warm trend of the WPWP water persisted.

Further support that the variabilities in the satellite data of the WPWP are real comes from the in situ expendable bathy thermograph (XBT) data for 1982 to 1990. Figure 3C shows a time series of Volunteer Observing Ship (VOS) XBT data for the WPWP. There is a monotonic increase in temperature between 1984 and 1988 and a fluctuation after 1988. This pattern is close to the results of our satellite data analysis. Generally speaking, nonuniformity of the XBT data distribution over the spatial and the seasonal time scales in the WPWP leads to biases in the analysis. Compared with satellite data, which are much more uniformly sampled, the relative scatter of the data points in the XBT plot may reflect these biases.

With the unprecedented temporal and spatial satellite MCSST observations, we have been able to conduct a year-to-year SST and area variability analysis for the WPWP. To quantify those changes, further study is especially needed to provide trustworthy analyses of the expected future global surface warming. Such satellite image analysis represents a useful tool for tracking the fluctuations in WPWP temperature and size from year to year. These satellite observations may provide new insight into the mechanisms responsible for the initiation and development of ENSO. They may also improve our understanding of upper-ocean processes, air-sea exchanges, and the global atmosphere.

REFERENCES AND NOTES

1. World Climate Research Programme, "Scientific Plan for the TOGA [Tropical Oceans and Global Atmosphere]-Coupled Ocean-Atmosphere Response Experiment," *WCRP Publ. Ser. No. 3* (1990).
2. R. Lukas and E. Lindstrom, "Proceedings of the Aha Haliko'a Hawaiian Winter Workshop on the Dynamics of the Ocean Surface Mixed Layer," *Hawaii Inst. Geophys. Spec. Publ.* (1987), pp. 67–94.
3. O. Brown and R. Evans, *J. Geophys. Res.* **90**, 11667 (1985).
4. X.-H. Yan, V. Klemas, D. Chen, *Eos* **73** (no. 4), 41 (1992).
5. G. C. Reid, *Nature* **329**, 142 (1987).
6. ______, *J. Geophys. Res.* **96**, 2835 (1991).
7. P. M. Kelly and T. M. L. Wrigley, *Nature* **347**, 460 (1990).
8. G. A. Wick and W. Emery, *J. Geophys. Res.* **97**, 5569 (1992).
9. Original MCSST data were processed by O. Brown. MCSST data were provided by the NASA Physical Ocean Distributed Active Archive Center at the Jet Propulsion Laboratory. Supported by NASA contract NAGW-2953 and NOAA contract NA26GP0257-01 from the Global Change Program.

7 August 1992; accepted 15 October 1992

EMF, an *Arabidopsis* Gene Required for Vegetative Shoot Development

Z. R. Sung,* A. Belachew, Bai Shunong, R. Bertrand-Garcia†

In higher plants, the transition from the vegetative to the reproductive state in the shoot meristem initiates flowering. To study this floral transition, a constitutively flowering mutant of *Arabidopsis thaliana* ecotype *columbia, embryonic flower* (*emf*), was characterized. No vegetative shoots were produced from *emf* embryos or calli; the shoot apical meristems (SAMs) in the *emf* embryos were altered compared to wild-type SAMs. The mutant SAMs enlarged precociously and produced inflorescence meristems upon germination. These results suggest that the dominant, wild-type allele *EMF* is required for the vegetative state of the SAM. In the absence of *EMF* function, the mutant embryo assumes the reproductive state.

The shoot apical meristem (SAM) is the origin of the shoot system; its cellular products differentiate as vegetative or reproductive organs. The SAM is formed during embryogenesis and can be identified by its terminal position and its tunica corpus cellular arrangements (*1*). However, little is known about how it is formed and how it functions. In *Arabidopsis* (*2, 3*), specific genes regulate meristem ontogeny (*4*) and fate determination (*5–7*). Here, we describe a mutant that identifies a gene, *EMF*, involved in the switch between the vegetative and the reproductive meristem.

Four independent *emf* mutants were recovered from ethyl methane sulfonate (EMS)– and gamma-ray–mutagenized *Arabidopsis* seeds by screening for individual plants that segregated 25% offspring with abnormal phenotypes (Fig. 1); the data presented are based on the characterization of the first mutant recovered from the EMS-mutagenized *Arabidopsis* seeds. The wild-type *Arabidopsis* is a semirosette plant (*8*). There is no internode elongation in the vegetative shoot until the onset of flowering. Whereas the heterozygous plants were indistinguishable from the wild-type plants, the homozygous *emf* plants did not produce a normal rosette upon germination but rather produced several cauline leaves and multiple floral buds (Fig. 1A) that later set fruits (Fig. 1B). Flowers of *emf* plants were

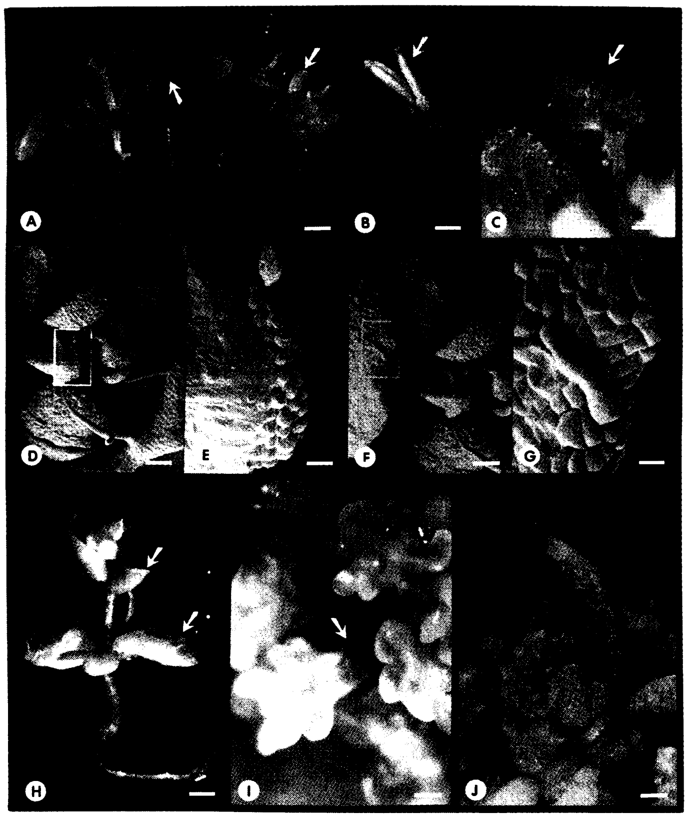

Fig. 1. (**A**) Normal (*EMF*, left) and mutant (*emf*, right) plants 18 days after germination. Seeds from a heterozygous plant were sterilized and vernalized for 3 days and then grown under 9 hours of light at 21°C on agar plates that contained half-strength Murashige and Skoog (MS) medium (*11*) without plant growth regulators. The normal plant is at the rosette stage with two cotyledons and four leaves; all have long petioles. The mutant has petioleless cotyledons and several sessile leaves and floral buds. Arrows point at the cotyledons. Bar = 1.0 mm. (**B**) Normal (bottom) and mutant (top) plants 6 weeks after germination under 9 hours of light per day. The *emf* mutant shows two fruits or siliques. Arrow points at the silique. Part of a normal plant (shown at the bottom) has rosette leaves with long petioles but no flowers. Bar = 1.1 mm. (**C**) Regenerating *emf* tissue on shoot-inducing medium (SIM), showing structures that resemble pistils. Root explants of *emf* seedlings were placed on callus-inducing medium [B5 medium (*11*) that contained 2,4-D (0.5 mg/liter) and kinetin (0.05 mg/liter)] for 4 weeks. Calli were transferred onto SIM [B5 medium + indole acetic acid (0.15 mg/liter)] and 2-isopentenyl adenine (5 mg/liter) for 6 weeks. Arrow points at papillae-like structures. Bar = 0.2 mm. (**D**) Scanning electron micrograph (SEM) of a mutant flower. Bar = 60.0 μm. The boxed area, enlarged in (**E**), shows the papillae on the pistil. Bar = 11.6 μm. (**F**) SEM of a mutant, showing the sepal-like structure. Bar = 59.9 μm. The boxed area, enlarged in (**G**), shows an elongated cell, characteristic of sepal cells. Bar = 11.8 μm. (**H**) A 20-day-old *emf* mutant plant showing inflorescence, two petioleless cotyledons, a small stem, cauline leaves, and several floral buds. Arrows point at the cauline leaves. Bar = 0.48 mm. (**I**) Regenerating *emf* tissue on SIM, showing flower-like structures. Arrow points at a small stem resembling the pedicel upon which whorled organs are situated. Bar = 0.2 mm. (**J**) Regenerating normal tissue on SIM, showing the rosette-like shoot. Bar = 0.61 mm.